Atmos. Meas. Tech. Discuss., 8, 10319–10360, 2015
www.atmos-meas-tech-discuss.net/8/10319/2015/
doi:10.5194/amtd-8-10319-2015

Atmospheric Measurement Techniques Discussions

Monitoring and tracking the trans-Pacific transport of aerosols using multi-satellite aerosol optical depth retrievals

A. R. Naeger[1], P. Gupta[2,3], B. Zavodsky[4], and K. M. McGrath[5]

[1]University of Alabama in Huntsville, Huntsville, AL, USA
[2]NASA Goddard Space Flight Center, Greenbelt, MD, USA
[3]University Space Research Association, MD, USA
[4]NASA Marshall Space Flight Center, Huntsville, AL, USA
[5]Jacobs Engineering Inc., ESSSA Group, Huntsville, AL, USA

Received: 20 July 2015 – Accepted: 9 September 2015 – Published: 7 October 2015

Correspondence to: A. R. Naeger (aaron.naeger@nasa.gov)

Published by Copernicus Publications on behalf of the European Geosciences Union.

Abstract

The primary goal of this study was to generate a near-real time (NRT) aerosol optical depth (AOD) product capable of providing a comprehensive understanding of the aerosol spatial distribution over the Pacific Ocean in order to better monitor and track the trans-Pacific transport of aerosols. Therefore, we developed a NRT product that takes advantage of observations from both low-earth orbiting and geostationary satellites. In particular, we utilize AOD products from the Moderate Resolution Imaging Spectroradiometer (MODIS) and Suomi National Polar-orbiting Partnership (NPP) Visible Infrared Imaging Radiometer Suite (VIIRS) satellites. Then, we combine these AOD products with our own retrieval algorithms developed for the NOAA Geostationary Operational Environmental Satellite (GOES-15) and Japan Meteorological Agency (JMA) Multi-functional Transport Satellite (MTSAT-2) to generate a NRT daily AOD composite product. We present examples of the daily AOD composite product for a case study of trans-Pacific transport of Asian pollution and dust aerosols in mid-March 2014. Overall, the new product successfully tracks this aerosol plume during its trans-Pacific transport to the west coast of North America. However, we identify several areas across the domain of interest from Asia to North America where the new product can encounter significant uncertainties due to the inclusion of the geostationary AOD retrievals. The uncertainties associated with geostationary AOD retrievals are expected to be minimized after the successful launch of the next-generation advanced NOAA GOES-R and recently launched JMA Himawari satellites. Observations from these advanced satellites will ultimately provide an enhanced understanding of the spatial and temporal distribution of aerosols over the Pacific.

1 Introduction

Although stricter emission control standards in the United States have led to a reduction in the domestic emissions of particulates since the 1980s, degraded air quality condi-

AMTD
8, 10319–10360, 2015

tions over the western United States have occurred due to foreign dust and pollution aerosols (Yu et al., 2012). For instance, the expanding cities and rapid industrialization of East Asia are major source regions of pollution emissions while biomass burning activities across Southeast Asia release smoke into the atmosphere (Streets et al., 2003). In addition, frequent dust storms originate from the Taklamakan and Gobi deserts in the late winter and early spring with a daily average dust emission of 1.58 million tons in April (Zhao et al., 2006). These smoke and dust aerosols combine with the other pollutants in a trans-Pacific transport that occurs frequently during late winter and early spring when the East Asian winter monsoon is near its peak strength (Gong et al., 2006). This East Asian winter monsoon brings cold, dry air outbreaks leading to strong surface winds that can efficiently pick up dust from the deserts. Once lofted in the atmosphere, the dust, smoke, and pollution aerosols are quickly transported to the western Pacific by a persistent offshore wind flow from the Asian continent (Talbot et al., 1997). Then, the aerosols are carried by strong mid- to upper-level westerly winds across the Pacific to the western United States where they can be transported from the free troposphere towards the ground, which can increase the risk of lung cancer and cardiopulmonary mortalities (Pope et al., 2002). Consequently, limiting domestic emissions in the United States alone is inadequate for limiting the aerosol effects on human health as the total mass of aerosols entering the United States from overseas is similar to that emitted domestically (Yu et al., 2012). Not only can aerosols degrade the air quality, but they can also have direct and indirect effects in the atmosphere through interacting with solar radiation and clouds which can have significant impacts on the climate and weather (e.g., Khain et al., 2005; Ault et al., 2011; Naeger et al., 2013a). Therefore, it is important that we continually monitor aerosols across the Earth, and determine their concentration and spatial variability, especially during the late winter and early spring period when the trans-Pacific transport of Asian aerosols occurs rather frequently.

A major issue when attempting to monitor aerosols across the Pacific is the large amount of cloud cover that often resides over this region. In fact, Mace et al. (2009) used merged data from the Cloud-Aerosol Lidar and Infrared Pathfinder Satellite Ob-

AMTD
8, 10319–10360, 2015

servations (CALIPSO) and Cloudsat satellite to show that cloud cover exceeded 90 % throughout the North Pacific between July 2006 and June 2007. Aerosol optical depth (AOD) retrievals should generally be avoided in cloudy regions due to the difficulty in separating the visible reflectance of the clouds and aerosols that lead to biases in the retrievals. Zhang et al. (2005) found that cloud contamination and cloud brightening lead to an overestimation of 10–20 % in the monthly averaged MODIS AOD over oceans. Although Zhang et al. (2005) used an outdated version of the AOD product, these AOD biases over ocean were still present in the Collection 5.1 product (Toth et al., 2013). The MODIS Collection 6.0 AOD product has been refined to solve some of the cloud contamination and cloud brightening issues in Collection 5.1 (Shi et al., 2014). Nonetheless, users should still be cautious of AOD biases due to clouds in the Collection 6.0 product since lingering issues are very likely to exist. Thus, cloud cover will continue to hinder our ability to monitor the trans-Pacific transport of aerosols when using observations from a passive low-earth orbiting satellite alone. The CALIPSO satellite carries the active Cloud-Aerosol Lidar and Orthogonal Polarization (CALIOP) instrument that can detect aerosol plumes above cloud layers (Winker et al., 2010). However, the extremely narrow field of view of CALIOP provides vertical curtain-like measurements that provide very limited information on the instantaneous spatial distribution of aerosols. Also, near-real time (NRT) CALIPSO measurements are unavailable. Therefore, aerosol information from CALIPSO will not benefit this study where we develop a NRT AOD product that helps monitor aerosol plumes across the Pacific.

In this study, we merge observations from low-earth orbiting (LEO) and geostationary (GEO) satellites in order to develop a NRT 6 hourly and daily AOD composite product centered over the Pacific Ocean. The new product will demonstrate the benefits of merging LEO and GEO satellite observations for tracking aerosol plumes in the atmosphere. In the following sections, we discuss the data products used in this study (Sect. 2), present the methodology for generating NRT AOD product (Sect. 3), show results from a case study of trans-Pacific transport of Asian aerosols (Sect. 4), discuss uncertainties (Sect. 5), and conclude with a summary and discussion (Sect. 6).

AMTD
8, 10319–10360, 2015

2 Data

In order to generate the NRT AOD product, we utilize the MODIS instrument onboard the LEO Aqua and Terra satellites. MODIS has 36 spectral bands with center wavelengths between 0.41 and 14.5 µm and spatial resolutions of 250, 500, and 1000 m. In general, the MODIS team retrieves AOD by comparing the reflectances from the solar bands to a lookup table of computed reflectances based on sun/satellite geometry, surface reflectance, and aerosol type (Remer et al., 2005). High quality AOD products have been under development by the MODIS team with the most recent release of the Collection 6 Level 2 AOD product (Remer et al., 2013). In this study, we actually use the Collection 5.1 Level 2 AOD product since a NRT version for Collection 6 has yet to be released as of January 2015. The Collection 5.1 release of MODIS dark target algorithm provides a 10 km AOD product with uncertainties over ocean and non-bright surfaces of $\pm 0.03 \pm 0.05 \times \mathrm{AOD}$ and $\pm 0.05 \pm 0.15 \times \mathrm{AOD}$, respectively (Remer et al., 2005; Levy et al., 2010). MODIS AOD is usually retrieved with rather low uncertainties due primarily to the availability of numerous spectral bands. For example, despite some lingering issues with cloud contamination in the MODIS AOD product, the cloud screening technique performs well in most instances due to the numerous spectral bands of MODIS that allows for the utilization of many different cloud detection tests. Each cloud detection test brings its own unique strength to the screening technique, such as the 1.38 µm band to detect thin cirrus clouds in the upper troposphere (Ackerman et al., 2006). Furthermore, the availability of the 0.47, 0.66, and 2.12 µm bands improves the estimation of surface reflectivity which helps reduce AOD uncertainties over dark land surfaces, such as vegetation and soils (Levy et al., 2007). This particular strength of the MODIS AOD retrieval algorithm will especially benefit the NRT AOD product when aerosols are over land surfaces. Note that the NRT version of the Collection 5.1 AOD product is distributed with an average latency of approximately 90 min via NASA's Land and Atmosphere Near real-time Capability for Earth observing system (LANCE) center.

AMTD
8, 10319–10360, 2015

In addition to MODIS, the NRT AOD product incorporates AOD retrievals from the Visible/Infrared Imager and Radiometer Suite (VIIRS) onboard the Suomi National Polar-orbiting Partnership (NPP) satellite. The VIIRS instrument with its 22 spectral bands was designed to continue the decade-long success of retrieving AOD from MODIS, therefore, the same strengths as just discussed for MODIS also apply to VIIRS. In fact, Liu et al. (2014) showed that AOD from the VIIRS aerosol Environmental Data Record (EDR) closely compares to MODIS AOD. Although VIIRS follows the same orbit-track as MODIS Aqua, it is capable of providing additional information on the spatial distribution of AOD due to a wider swath width and higher spatial resolution at swath edge compared to MODIS (Hillger et al., 2013). VIIRS has a swath width of 3000 km vs. 2330 km for MODIS and a spatial resolution at swath edge of approximately 1.5 km vs. 5 km for MODIS. We process AOD data from the VIIRS aerosol EDR via the NOAA Comprehensive Large Array-Data Stewardship System (CLASS) subscription service. However, the VIIRS AOD product via NOAA CLASS has approximately a seven hour latency compared to the 90 min latency of MODIS AOD via NASA LANCE. Consequently, VIIRS retrievals are only incorporated into our daily AOD composite product, but not into our 6 hourly composite product.

Even though the advanced MODIS and VIIRS instruments provide high-quality AOD retrievals, they fly onboard LEO satellites that observe the same location only once per daytime period. Thus, cloud cover can lead to large gaps in the coverage of AOD when only analyzing data from instruments onboard LEO satellites, especially over the generally cloudy Pacific Ocean. To mitigate this issue and more effectively track the trans-Pacific transport of aerosols, we incorporate the high temporal resolution measurements from the NOAA GOES-15 and Japan Meteorological Agency (JMA) MTSAT-2 geostationary platforms into the NRT AOD product. This study uses the Northern Hemisphere scan modes with a 30 min temporal resolution for both GOES-15 and MTSAT-2. Because of the high temporal resolution, a cloud feature that might be present in the MODIS and VIIRS overpasses may propagate out of the scene for subsequent GOES-15 or MTSAT-2 observations allowing for a successful AOD retrieval and an increase

AMTD
8, 10319–10360, 2015

in AOD coverage. The major downside of the instruments onboard the GOES-15 and MTSAT-2 is that they only have 5 spectral bands, consisting of one visible and four infrared bands, with spatial resolutions of 4 and 5 km for the infrared bands, respectively. As a result, AOD retrievals from these satellites will typically have higher uncertainties than those from MODIS as shown by the validation study of Paciorek et al. (2008) where the GOES AOD uncertainty range over dark land surfaces was 18–34 % with lower values expected over water. Note that easily accessible archives containing AOD data are unavailable for the GOES-15 and MTSAT-2 satellites, therefore, we develop our own retrieval algorithms for these satellites. The GOES AOD retrieval algorithm developed for this study is similar to the GOES Aerosol/Smoke Product (GASP) discussed in Prados et al. (2008). The latency of our GOES and MTSAT AOD retrievals are typically less than 30 min. Table 1 provides a detailed summary of the different satellites and aerosol retrievals used in producing the NRT AOD product.

In this study, we use ground-based instrumentation at the AErosol RObotic NETwork (AERONET) stations to assist with developing accurate AOD retrieval algorithms for the GOES and MTSAT satellites. AERONET stations are located throughout the globe, but we focus on 10 of those set across eastern Asia since aerosols usually propagate over this region prior to their trans-Pacific transport. The sun-sky radiometer instruments at the AERONET stations provide very accurate measurements of aerosol optical properties from the ultraviolet to the near-infrared (Holben et al., 1998). We utilize AOD and single scattering albedo data at 500 and 675 nm, and we derive the AOD at 550 nm via the angstrom exponent. Reported uncertainties for the Level 2.0 cloud-screened and quality-assured AOD and single scattering albedo data are approximately 0.01–0.015 and 0.03–0.07, respectively (Schmid et al., 1999; Dubovik et al., 2000). At the time of this study, Level 2.0 data is not available at a number of AERONET stations across East Asia, therefore, we utilize the Level 1.5 cloud-screened data for these particular stations.

We also utilize AOD retrievals from the Multi-angle Imaging SpectroRadiometer (MISR) onboard EOS Terra satellite to compare against the NRT AOD product. The

AMTD
8, 10319–10360, 2015

MISR instrument observes the earth in four spectral bands (0.446, 0.557, 0.671, 0.866 µm) and has nine cameras operating at nine different angles, four in forward, four in backward and one in nadir direction. Its swath width is about 360 km (Diner et al., 2002), and due to the narrow swath width, near global coverage is obtained in 8–9 days at the equator and 2 days near the poles. The relevant MISR data set for this paper is the level 2 aerosol data (MIL2ASAE) containing AOD at 4 spectral channels. The level 2 AODs retrieved in 17.6 km × 17.6 km spatial resolution at 0.56 µm have been gridded to 0.5° × 0.5° resolution for the comparison purpose. A detailed description of the aerosol algorithm is given in Kahn et al. (Kahn et al., 2005). MISR AOD over ocean validated using Maritime Aerosol Network (MAN) and found that that MISR AODs are positively biased by about 0.04 with respect to surface measured AODs (Witek et al., 2013).

Finally, the Cloud-Aerosol Lidar and Infrared Pathfinder Satellite Observations (CALIPSO) carries an active lidar that emits pulses of energy at 532 and 1064 nm to produce vertical, curtain-like images of the atmosphere (Winker et al., 2003). CALIPSO has the unique ability to measure aerosols above clouds, therefore, we use the level 1B 532 attenuated backscatter profiles to help confirm areas of high AOD among clouds in the AOD composite product. In addition, CALIPSO measures the height of aerosols in the atmosphere, which we use as an input into the NOAA Hybrid Single Particle Lagrangian Integrated Trajectory Model (HYSPLIT) to forecast the transport path of Asian aerosols. Note that AERONET, MISR, and CALIPSO data are only used to help validate and develop our AOD composite product. In other words, AOD retrievals from these instruments are completely independent of our product.

3 Methodology

To generate the NRT AOD product, we proceed through three major tasks. First, we perform AOD retrievals and cloud clearing techniques for each GOES and MTSAT northern hemispheric scan modes. Second, we gather and process all valid MODIS

AMTD
8, 10319–10360, 2015

and VIIRS AOD data. Third, the GOES, MTSAT, MODIS, and VIIRS AOD retrievals are placed onto the same domain with a $0.5^\circ \times 0.5^\circ$ grid spacing. In this section, we discuss each of these tasks, but place much of the focus on the first major task as it required a large amount of effort to complete.

The general flow of the GOES and MTSAT AOD retrieval algorithms are outlined in Fig. 1. In order to effectively describe the retrieval algorithms, we present an example of how AOD is retrieved for a MTSAT-2 image on 18 March 2014 at 05:01 UTC. The first step is to gather MTSAT-2 visible images at 05:01 UTC beginning 19 February through 18 March (28 total), and convert the nominal reflectance (ρ_{nom}) to a calculated reflectance using the monthly linear regression coefficients provided by the Meteorological Satellite Center of JMA via a vicarious calibration technique. Equation (1) demonstrates how the ρ_{nom} is converted to the calculated or satellite reflectance (ρ_{sat}) where C_0 and C_1 are the intercept and slope linear

$$\rho_{\text{sat}} = \frac{(C_0 + C_1 \cdot \rho_{\text{nom}}) \cdot d^2}{\theta_0} \quad (1)$$

regression coefficients, d is the Earth–Sun distance in astronomical units, and θ_0 is the solar zenith angle. The linear regression coefficients for March 2014 are 1.2257 and −0.0006 for C_0 and C_1, respectively. After calculating ρ_{sat} for each MTSAT-2 image, we find the second lowest ρ_{sat} for each pixel during the 28 day period which generates the clear-sky background (ρ_{min}) image. The same approach is taken to generate the ρ_{min} for GOES-15 except that the ρ_{sat} is calculated based on calibration coefficients provided by the NOAA NESDIS Center for Satellite Applications and Research (STAR). Note that we chose the 28 day period after conducting sensitivity tests using 21, 24, 28, and 35 day periods which is discussed in Sect. 5. Although our sensitivity tests indicated that 28 days is the optimal period, the variation in solar geometry throughout the four week period can still lead to considerable uncertainties, especially at lower surface reflectances.

AMTD
8, 10319–10360, 2015

For the second step, we retrieve the surface reflectance (R_{sfc}) by removing the atmospheric effects from the ρ_{min} image via a look-up table (LUT_{sfc}). The LUT_{sfc} is generated using the Version 1.1 of the Second Simulation of a Satellite Signal in the Solar Spectrum Vector (6SV) code. The highly accurate 6SV radiative transfer code (Kotchenova et al., 2006; Kotchenova and Vermote, 2007) contains the same atmospheric correction procedure used by the MODIS team (Vermote and Kotchenova, 2008). However, in developing the LUT_{sfc}, we are required to make some assumptions regarding the state of the atmosphere throughout the ρ_{min} image. First, in order to remove the atmospheric effects, the 6SV requires temperature, water vapor, and ozone information throughout the atmosphere. We determined that the US standard profiles provided the most appropriate information based on the close agreement between the climatological average air temperature in April over the Northern Hemispheric Pacific Ocean of 285 K and the US Standard 1013 hPa temperature of 288 K (Jones et al., 1999). Second, we assume a background AOD of 0.05 since the visible bands onboard the MTSAT-2 and GOES-15 satellites have been shown to be insensitive to low concentrations of AOD (Knapp et al., 2005). We chose the 6SV continental and desert aerosol models to represent the optical properties of the aerosols, and we discuss the reasons for selecting these models in the next paragraph. After making these assumptions, the 6SV code is used to simulate the top of atmosphere reflectance (ρ_{toa}) values for a range of $16\theta_0$, 16 viewing zenith angles (θ), 15φ, and $8R_{sfc}$ (i.e., LUT_{sfc}). We search the LUT_{sfc} for the solar/satellite geometry that most closely matches that for each pixel in the MTSAT-2 and GOES-15 image. After identifying the solar/satellite geometry match, we retrieve the R_{sfc} for each pixel by interpolating ρ_{min} to the simulated ρ_{toa} values. Figure 2a displays the MTSAT-2 ρ_{sat} image on 18 March 2014, where a plume of dust and pollution extending from China to over the Sea of Japan trails behind a frontal band associated with a low-pressure system near Japan. The R_{sfc} retrievals for each pixel in the MTSAT-2 image are shown in Fig. 2b where we only retrieve the R_{sfc} when the θ_0 and θ is less than 70° as AOD retrievals at larger angles are associated with significant uncertainty (e.g., Ignatov and Stowe, 2002). Also, AOD is not retrieved for the pixels highlighted

AMTD
8, 10319–10360, 2015

in red ($R_{sfc} > 35\,\%$), since they are likely contaminated with either cloud, snow, or ice. However, we are able to attempt an AOD retrieval for the majority of the pixels in the R_{sfc} image as most of the scene appears to be uncontaminated.

The third step consists of retrieving the GOES and MTSAT AOD via a second LUT based on the 6SV continental aerosol model. This second LUT (i.e., LUT_{cont}) is created similar to LUT_{sfc} except that the 6SV code is used to simulate the ρ_{toa} for 7 different AODs in addition to the range of θ_0, θ, φ, and R_{sfc} that created LUT_{sfc}. The most significant assumption in creating the LUT_{sfc} is the selection of the aerosol model as the simulated ρ_{toa} can vary greatly based on the optical properties of the aerosols. Thus, prior to selecting an aerosol model for our domain, we conduct a detailed comparison between the observed ρ_{sat} and simulated ρ_{toa} using seven different 6SV aerosol models for 24 unique cases occurring over AERONET stations across eastern Asia during March and April 2014. For each case, we provide the 6SV with the R_{sfc} retrieval value closest to the AERONET station along with precise values of θ_0, θ, and φ from the MTSAT-2, and 550 nm AOD from AERONET data. Then, we simulate the 6SV using these identical input values and compare the ρ_{toa} values to the ρ_{sat} from MTSAT-2 in order to determine the most appropriate aerosol model. Figure 3 presents the results from each aerosol model for the 24 cases where the continental model (red) simulated the most realistic ρ_{toa} values as ρ_{sat} was slightly overestimated at values less than about 16 % and underestimated at values greater than about 20 %. The average difference between ρ_{sat} and ρ_{toa} for the 24 cases was only −0.09 % when using the continental model leading to the lowest root mean square (RMS) error of 1.31 % (Table 1). As a result, we retrieve AOD based on the LUT_{cont} by determining the most appropriate R_{sfc} in the table and then interpolating ρ_{sat} to the simulated ρ_{toa} values to retrieve the AOD. However, the continental aerosol model performed poorly for a couple distinct cases involving pure dust emitted from the Taklamakan and Gobi Deserts. This prompted us to create another LUT based on the 6SV desert aerosol model (i.e., LUT_{dust}), but we do not invoke the LUT_{dust} unless the pixel passes a handful of dust detection techniques that are explained in the following paragraph. Note that separate

AMTD
8, 10319–10360, 2015

LUTs were generated for the visible bands of the MTSAT-2 and GOES-15 due to having unique spectral response functions. The spectral response functions for the visible bands onboard these satellites were not available in the 6SV1.1 RTM, therefore, we updated the 6SV source code to account for these bands prior to producing the LUTs.

For the fourth and final step of the MTSAT and GOES retrieval algorithms, we use cloud and dust detection procedures to disregard contaminated AOD retrievals and identify any pixels influenced by dust. Developing accurate cloud detection algorithms for these GEO satellites is not a trivial task due to their lower spatial resolution and limited number of spectral bands. In an effort to obtain as much information as possible from 4 spectral bands (6.7 µm water vapor band is not used), we extract reflectance and temperature from the 3.9 µm band based on Mecikalski et al. (2010). Then, we use spectral, spatial, and temporal techniques based on the reflectance and temperature information from the 4 spectral bands to identify clouds and dust in each satellite image. The cloud/dust detection techniques for these satellites are similar even though GOES has a 13.3 µm band instead of the 12.0 µm band onboard MTSAT. However, we were able to develop more sophisticated dust detection techniques for MTSAT since dust has a unique spectral signature in the 10.8 and 12.0 µm bands (Ackerman et al., 1997; Sokolik, 2002; Naeger et al., 2013b). In this paper, we will only briefly step through the MTSAT cloud/dust detection procedure (Table 3), but will note any important differences that arise in the GOES procedure. The techniques shown in Table 3 were developed after close examination of dozens of MTSAT satellite images involving cloud and aerosols throughout the year 2014. Thus, this procedure can be applied during any season, but note that it will generally overestimate cloud coverage as its main purpose is to limit sub pixel cloud contamination and cloud adjacency effects from impacting the AOD retrievals. The spatial techniques help greatly with disregarding AOD retrievals impacted by these cloud effects over both land and ocean, but they work especially well over the homogeneous ocean surface where the thresholds for cloud detection were able to be set to lower values.

AMTD
8, 10319–10360, 2015

Figure 2c shows the overall results of the cloud/dust procedure for θ_0 and $\theta < 75^\circ$ on 18 March 2014 at 05:01 UTC. We run the procedure in the same order as shown in Table 3. After passing one of the spectral, spatial, or temporal techiques, the pixel is immediately labeled as cloud using the corresponding number in the right-hand column. A pixel must fail all the cloud detection techniques to be labeled cloud-free. We only retain AOD retrievals that are associated with cloud-free pixels. Approximately 80 % of the valid MTSAT pixels are labeled as cloud and the spectral techniques detect about 71 % of these clouds. Spectral technique #3 does not appear in the GOES cloud/dust procedure due to the absence of the 12.0 µm band. The spatial techniques detect a significant fraction of the remaining clouds (∼ 28 %), especially in regions of scattered cumulus clouds over the ocean. Although the impact of the temporal techniques appears very minimal in Fig. 2c, they are able to detect some lingering clouds (e.g., ∼ 40° N, 120° E) that could lead to artifacts in the NRT AOD product. A small portion of the pixels are labeled as cloud when they are actually cloud-free sunglint pixels (∼ 4° N, 125° E), but this is not an issue in this study as sunglint regions cause high biased AOD retrievals.

Since possible dust regions can be mislabeled as cloud by our procedure due to their similar spectral characteristics, we use four special dust techniques to locate pixels mislabeled as cloud and relabel them as cloud-free. The special techniques were developed based on the fact that dust regions can have strong positive 3.8–10.8 µm values similar to clouds, but are often more homogeneous than clouds while influencing 10.8–12.0 µm values less than −1 K. A considerable number of pixels are relabeled as cloud-free in northern China. The final dust technique in Table 3 operates only on cloud-free pixels. If a pixel passes this technique, then the AOD is revised based on the LUT_{dust} instead of the LUT_{cont} that was assumed for each pixel during the third step. Although similar to MTSAT, the GOES dust detection technique is not as robust due to the nonexistent 10.8–12.0 µm test. After applying the cloud/dust detection procedure, we arrive at our final cloud-cleared AOD map for this MTSAT scan at 05:01 UTC on 18 March (Fig. 2d). The map shows high AOD > 1.0 associated with the thick pollution

AMTD
8, 10319–10360, 2015

and dust plume propagating from eastern Asian to over the Pacific Ocean. Pollution and smoke plumes are also causing high AOD in regions across southern Asia. Thus, we are able to depict some features on this AOD map, but the large gaps in coverage due to clouds make it difficult to fully understand the spatial distribution of aerosols.

To obtain a more complete picture of the aerosol spatial distribution, we create daily AOD composites that combine information from MTSAT, GOES, MODIS, and VIIRS over a 24 h period beginning 12:00 UTC each day. During each 24 h period, our automated scripts continually search for the most recent GOES and MTSAT northern hemispheric scan data files (Table 1). Once a new file is downloaded, it only takes several minutes for the GOES or MTSAT retrieval algorithms to process the files and generate a cloud-cleared AOD map. Also, during this period, our scripts actively download the most recent MODIS and VIIRS AOD data (Table 1) from the NASA LANCE and NOAA CLASS data systems, respectively. At the end of the valid 24 h period, we combine the AOD information from all sensors onto a common $0.5^{\circ} \times 0.5^{\circ}$ grid domain centered over the central Pacific Ocean in order to effectively track the trans-Pacific transport of aerosols. The rather coarse $0.5^{\circ} \times 0.5^{\circ}$ grid is suitable for our particular application where larger scale, more homogeneous aerosol plumes are the focus. We use a nearest neighbor approach to find all AOD retrievals for each sensor that fall within a grid box, and calculate separate averages for the GEO and LEO sensors. In order to prevent poor quality MODIS AOD retrievals from being introduced into our AOD composite maps, we use the MODIS cloud fraction parameter and quality assurance flags to ignore retrievals associated with cloud cover > 70 % and marginal confidence. To disregard poor quality VIIRS AOD we ignore retrievals when at least one pixel among the 8×8 pixel region is cloud or cirrus contaminated as indicated by the quality flags provided in the product. We already performed extensive quality control and cloud clearing procedures for the GOES and MTSAT retrievals, thus, we do not disregard any additional data prior to calculating the average for the GEO sensors. When AOD retrievals from both GEO and LEO sensors populate a grid box, the average AOD based on the LEO sensors is chosen to represent the box due to the higher uncertainty associ-

AMTD
8, 10319–10360, 2015

ated with the GOES and MTSAT retrievals (Table 1). After this final operation, the AOD composite maps are generated and disseminated for analysis.

In this study, we group together the AOD from the GEO and LEO sensors due to the similarity between the different sensors and retrieval algorithms. For instance, we develop very similar AOD retrieval algorithms for the GOES and MTSAT satellites, which use the same continental aerosol type and LUT approaches. As a result, AOD from the GEO sensors are expected to be comparable as they encounter similar uncertainties over water and land regions. Nevertheless, there will be a small number of instances when both GOES and MTSAT AOD retrievals fall within the same grid box due to the limited overlap between their geographical coverage. For the MODIS and VIIRS sensors, we do not retrieve AOD, but instead process the AOD from the data products available through the NASA LANCE and NOAA CLASS data systems. Although the VIIRS AOD retrieval algorithm is based on the MODIS algorithm, there are some significant differences between them as they use different bands, and have unique cloud mask and internal screening tests (Jackson et al., 2013). Nevertheless, Liu et al. (2014) conducted an extensive validation of VIIRS AOD against the Maritime Aerosol Network (MAN) where they found that 71 % of VIIRS retrievals were within the expected uncertainty range applied to MODIS retrievals over ocean. We also found a close agreement between MODIS and VIIRS AOD after qualitatively comparing the two sensors for numerous scenes over the Pacific Ocean. Therefore, we do not expect significant issues when averaging the MODIS and VIIRS AOD retrievals for generating our AOD composite product. In our current methodology, we do not apply techniques to account for the differences in observation times or spatial resolutions between the GEO and LEO sensors, which may lead to undesirable jumps in AOD when merging the different sensors on a common grid. However, our simplified approach does not appear to lead to frequent jumps in AOD in our daily composite product as will be indicated by the case studies in Sect. 4. We plan to develop more advanced methodologies in the future for merging AOD information from the next-generation NOAA GOES-R and recently launched JMA Himawari satellites. Our primary goal here is to develop and evaluate

AMTD
8, 10319–10360, 2015

a simple methodology that shows the application of merging AOD from current GEO and LEO satellite sensors.

4 Results

4.1 18 March 2014

The top three panels in Fig. 4 display the daily AOD composites for the case study on 18 March 2014. The product is valid at 00:00 UTC on this day since it was created by using satellite AOD information between 12:00 UTC on 17 March and 12:00 UTC on 18 March. Figure 4a is an example of the daily AOD composite with only MTSAT/GOES retrievals while Fig. 4b is an example with only MODIS/VIIRS retrievals. All these satellite retrievals are combined onto the same map to generate the final version of the daily AOD composite product, which shows a more complete picture of the spatial distribution of aerosols during this 24 h period (Fig. 4c). A massive aerosol plume extends from eastern China to almost the central Pacific region as moderate AOD of approximately 0.6 is identified around 38° N 165° E. Some moderate to thick aerosols are still propagating from the central China region behind the extensive cloud feature in the MTSAT 0.68 µm image suggesting that poor air quality and visibility may plague eastern China in the short-term. A fairly extensive aerosol plume appears to be moving from southeast China to the tropical Pacific and aerosol activity is high throughout much of Southeast Asia. It is important to note that the MTSAT/GOES retrievals blend into Fig. 4c rather well due to the overall good agreement in the spatial patterns of AOD between Fig. 4a and b. For example, the aerosol plume moving from Southeast China to the tropical Pacific is not fully represented using MODIS/VIIRS AOD retrievals alone. Fortunately, the MTSAT retrievals fill this region with AOD that blends in very well with the surrounding MODIS/VIIRS AOD. Also, the massive aerosol plume from eastern China is more fully represented in Fig. 4c than in Fig. 4b since MTSAT is able to observe additional cloud-free regions among the plume.

AMTD
8, 10319–10360, 2015

Although the spatial patterns of AOD compare fairly well between Fig. 4a and b, some important differences exist between the maps. The MTSAT/GOES AOD map fails to represent the region of moderate AOD identified in the MODIS/VIIRS map around 38° N 165° E. This region is nearly outside the viewing range of GOES but well within the viewing range of MTSAT. However, MTSAT is unable to find a cloud-free pixel among this region of broken clouds (Fig. 2a) due to its relatively coarse spatial resolution of 5 km at nadir. The much finer spatial resolution of the MODIS (~ 0.5 km at nadir) and VIIRS visible channels (~ 0.74 km at nadir) allows retrievals to be performed in cloud-free regions. Furthermore, MTSAT/GOES AOD is biased low and high depending on whether the retrieval is poleward and equatorward of 30° N, respectively, by an average of 0.02 compared to MODIS/VIIRS. However, regions of larger discrepancies are apparent when comparing Fig. 4a and b. For instance, MTSAT AOD is about 0.2 lower than MODIS/VIIRS around 30° N 137° E. The MODIS/VIIRS AOD in this area is generally within ±0.05 of the MISR AOD (Fig. 4e) while MTSAT is lower than MISR by −0.05 to −0.20 (Fig. 4d). The closer agreement between MISR and MODIS/VIIRS AOD suggests that the LEO retrievals are more accurate than MTSAT. Note that MISR retrievals are strictly for intercomparison purposes and completely independent of the AOD composite product. This tendency of MTSAT/GOES to be biased low is primarily caused by cloud cover influencing the ρ_{min} image which then leads to overestimations in the R_{sfc} retrievals (Fig. 2b). Clouds tend to impact the R_{sfc} retrievals more often in the north and central Pacific as the MTSAT/GOES spatial resolution decreases. On the other hand, the high bias over the tropical Pacific is mostly due to cloud contamination influencing the MTSAT AOD retrievals, which is evident by the areas of AOD > 1.0 appearing over parts of the tropical western Pacific. Neither MODIS/VIIRS or MISR depict these same areas of AOD > 1.0. There are large discrepancies between AOD retrievals across portions of Southeast Asia as indicated by the MISR overpass around 15° N 107° E. MODIS/VIIRS AOD is generally between 0.5 and 0.7 in this region, which is higher than MISR AOD by values of up to 0.3. MTSAT shows AOD values reaching 1.0 in some locations that are considerably higher than MODIS/VIIRS and MISR. When

AMTD
8, 10319–10360, 2015

comparing MTSAT to MISR alone, MTSAT AOD is 0.2 to 0.6 higher than MISR across Southeast Asia. These large differences in AOD across the region make it very difficult to assess the MTSAT retrievals using passive satellites alone. The very uncertain AOD retrievals can be attributed to the highly complex terrain of Southeast Asia along with the scattered cloud coverage on this day. Fortunately, it is very unlikely that any aerosol plumes originating from this region will undergo trans-Pacific transport.

The CALIPSO made several transects directly over the aerosol plumes across the western Pacific and eastern Asia on 18 March. We analyze the CALIPSO transects indicated in Fig. 4c (black lines) from east to west. Figure 5a shows the 532 nm attenuated backscatter profiles from about 03:20 UTC on 18 March where moderate backscatter values are measured from an aerosol plume at approximately 3 km in height (box 1). The CALIPSO Vertical Feature Mask (VFM) and aerosol subtype browse images confirmed this region of moderate backscatter as aerosol consisting of dust and polluted dust. This aerosol layer is likely interacting with the high, thick clouds to the north in Fig. 5a. The daily AOD composite product (Fig. 4c) reveals moderate to high AOD in the vicinity of this aerosol layer. Several noteworthy aerosol plumes are measured by CALIPSO during the transect at about 05:00 UTC (Fig. 5b). First, moderate backscatter values are associated with an aerosol layer from about 18–24° N (box 2). Even though the CALIPSO transect shows scattered low clouds residing beneath much of the aerosol layer, the AOD composite is still able to depict AOD ranging from 0.3 to 0.7 in this same area. Second, CALIPSO measures very strong backscatter signals from the aerosol region in box 3, which is clearly shown in the composite product by the large area of AOD > 1. The CALIPSO aerosol subtype algorithm labels this aerosol region as a mixture of dust and polluted dust. Lastly, CALIPSO measures moderate backscatter from a fairly thin aerosol plume mixed with smoke and polluted dust in box 4. A close inspection of the AOD composite reveals a confined area of AOD ~ 0.3 in the vicinity of the aerosol plume. A couple hours later at about 06:40 UTC CALIPSO flew directly over the very complicated scene of Southeast Asia (Fig. 5c) consisting of clouds located within an aerosol layer (box 5) and then aerosols above terrain fea-

AMTD
8, 10319–10360, 2015

tures (box 6). The CALIPSO VFM image revealed that portions of the aerosol layer in box 5 were cloud-free, especially near 10° N. CALIPSO measures moderate to high backscatter in these cloud-free regions, which suggests that the AOD > 0.5 shown in the AOD composite represents the aerosol activity across this region rather well. Thus, it is very likely that MISR is severely underestimating the AOD in this region while the MODIS/VIIRS and MTSAT AOD retrievals are performing much better. Lower backscatter is measured by CALIPSO over the terrain features in box 6, and the AOD composite shows lower AOD ranging from 0.4 to 0.5 in this same area. Overall, the CALIPSO transects indicate the AOD composite is capable of representing the intensity of the aerosol plumes throughout western Pacific and Asia.

4.2 HYSPLIT trajectory analysis

Now we investigate the transport pathways for three of the aerosol plumes identified in the CALIPSO 532 nm attenuated backscatter profiles (boxes 1, 2, and 5). We use the profiles to estimate the height of the three aerosol plumes, which are all around 3 km. The height is provided as an important input into the NOAA HYSPLIT model along with latitude and longitude information for each plume. We use HYSPLIT to run an ensemble of 24 trajectories from each aerosol plume location for a 96 h period beginning at 05:00 UTC on 18 March until that same time on 22 March. Nearly all the HYSPLIT trajectories initialized from position 1 (box 1) propagate the dust/pollution plume to over the far eastern extent of the Pacific Ocean or over the Pacific Northwest by 22 March at 05:00 UTC (Fig. 6). This dust/pollution plume is an excellent example of a typical trans-Pacific transport pathway via the midlatitude westerly winds (Wilkening et al., 2000). The ensemble of trajectories initialized from position 2 (box 2) suggest the aerosol plume is likely to move westward. A handful of trajectories show the plume moving slowly eastward, but they never make any significant headway toward North America by the end of the 4 day period. Position 5 (box 5) is not indicated on Fig. 6 as it was located over Southeast Asia and all the forward trajectories took the aerosol plume south and west of the initial position, thus, the trajectories never entered the

AMTD
8, 10319–10360, 2015

Google Earth display region. Consequently, the possible discrepancies in AOD that can appear over Southeast Asia are not considered a significant problem when using the AOD composites to track the trans-Pacific transport of aerosols.

4.3 23 March 2014

To confirm whether this dust/pollution plume reached the western coast of North America we generated the daily AOD composite valid at 00:00 UTC on 23 March (Fig. 7c). The daily AOD composite depicts moderate AOD of 0.4 to 0.5 over the extreme eastern Pacific, which suggests that remnants of the dust/pollution plume in the western Pacific were transported across the vast ocean. However, the HYSPLIT model was too aggressive in predicting the transport of the aerosol plume as indicated in Fig. 6 where the aerosol plume is already over the landmass of North America by 22 March at 05:00 UTC. This case study shows the utility of the AOD composites for model validation and the potential benefit of using the composites for model assimilation.

The overall results of the panels in Fig. 7 are very similar to that already discussed for the 18 March case. Again, the MTSAT/GOES retrievals (Fig. 7a) blend nicely into the MODIS/VIIRS AOD map (Fig. 7b) to generate a more robust spatial distribution of aerosols. Many of the same features are revealed on the MTSAT/GOES and MODIS/VIIRS AOD maps, such as the dense aerosol plume over eastern Asia. However, the full extent of the plume is shown when introducing the MTSAT retrievals into the AOD composite product. The MTSAT/GOES AOD map also reveals some aerosol activity over northern China that is not indicated on the MODIS/VIIRS map. CALIPSO measured a fairly large region of moderate backscatter from dust aerosols during a nighttime transect over northern China ($\sim 40^{\circ}$ N 106° E) on 23 March at about 19:00 UTC (not shown), which suggests that MTSAT is accurately representing the aerosol activity over this region. Over the extreme eastern Pacific, GOES retrieves moderate AOD for the transported dust/pollution plume, but MODIS/VIIRS is able to retrieve a larger region of AOD associated with this plume due to their significantly higher spatial resolution in these northerly locations. MTSAT/GOES retrievals appear

AMTD
8, 10319–10360, 2015

to encountering issues in similar areas as mentioned when analyzing the 18 March case. The MTSAT/GOES AOD retrievals are biased high compared to MODIS/VIIRS across the tropical Pacific, especially in the latitude band from 10–20° N over the eastern Pacific. However, some of the areas of elevated AOD around 0.3 depicted in the MTSAT/GOES map correspond well to that shown in the MODIS/VIIRS map (e.g., ~ 15° N, 165° W). MTSAT AOD is significantly lower than MODIS/VIIRS along the coast of southeast China (~ 25° N, 115° E) due to persistent cloud cover in this area throughout the 28 day period used to retrieve R_{sfc}. Large discrepancies between MTSAT and MODIS/VIIRS AOD are once again appearing in areas throughout Southeast Asia and eastern India.

To quantitatively show the gain in spatial coverage due to the inclusion of the GEO sensors in our daily AOD composite maps we calculate the number of valid AOD retrievals along with the percent coverage of those retrievals based on the total number of available grid boxes (70 400 grid boxes) across our composite domain. These statistics are calculated for the daily AOD composite maps when only LEO (MODIS/VIIRS) and GEO (MTSAT/GOES) sensors are considered and when both LEO and GEO sensors are considered in developing our final product. We show statistics for a six day period, which includes the 18 and 23 March case studies presented in this paper (Table 4). Overall, the LEO sensors provide more spatial coverage compared to the GEO sensors (67 % vs. 60 %) during this six day period. As shown in this paper, the higher percentage for the LEO sensors is partly due to the fact that they have better coverage throughout the northern regions of the AOD composite domain. The LEO sensors also have better coverage over the central Pacific and over the far eastern and western portions of the composite domain, which is due to the limited geographical coverage of the GEO sensors. The GEO retrieval algorithms developed in this study further limit their geographical coverage by restricting θ to less than 70° to avoid the very large uncertainties that arise at these oblique angles. Although the LEO coverage is better than GEO, introducing the GEO sensors into the AOD composite maps still leads to considerable increases in spatial coverage for our final product. For the six day period

AMTD
8, 10319–10360, 2015

in Table 4, the inclusion of the GEO sensors improves the spatial coverage of AOD from 67 % for the LEO sensors to 81 % for our merged LEO/GEO product. The GEO sensors lead to an improvement in the spatial coverage of AOD as their high temporal resolution allows for the identification of more cloud-free regions where a valid AOD can be retrieved.

5 Uncertainties

Although cloud contamination causes very scattered areas of anomalously high AOD among the MTSAT/GOES AOD retrievals, the most significant source of uncertainty is associated with the R_{sfc} retrievals. We tested how much uncertainty can be associated with the R_{sfc} retrievals due to the variation in solar geometry throughout the 28 day period. Overall, we found that the uncertainty in AOD increases with decreasing R_{sfc} values. For instance, the AOD uncertainty can be as high as 17 % at R_{sfc} values of 10 % but increase to almost 34 % at R_{sfc} values of 5 %. Note that these values represent the maximum possible uncertainty that can be associated with a cloud-free R_{sfc} retrieval. Nevertheless, this uncertainty is the most likely explanation for the MTSAT/GOES AOD bias found over portions of the Pacific Ocean on 18 and 23 March. When attempting to use a 21 and 24 day period for the R_{sfc} retrievals, we noticed major issues with cloud contamination that led to significant underestimations in AOD.

We found that the 6SV continental aerosol model was the most appropriate model for retrieving MTSAT/GOES AOD, since desert dust storms often mix with pollution when progressing eastward over the populated regions of Asia. Single scatter albedo retrievals from the AERONET stations across eastern Asia were often around 0.90 at 500 nm with a decreasing trend at larger wavelengths, which compared well to the prescribed single scattering albedo of the continental model. Conversely, the prescribed single scattering albedo values in the desert model are around 0.92 at 500 nm and increase with larger wavelengths. Thus, the desert model typically leads to underestimations in AOD across eastern Asia and the Pacific as it causes high biases in the

AMTD
8, 10319–10360, 2015

simulated reflectance at the top of atmosphere. However, single scatter albedo retrievals from AERONET stations located in the desert regions of China were in better agreement to the 6SV desert model (not shown), which explains why we incorporated this model into the AOD retrieval algorithm.

Finally, we validated the daily AOD composite on 18 March 2014 (i.e., Fig. 5c) against level 1.5 AERONET AOD from 10 stations in East Asia and 4 stations along the west coast of the United States (Fig. 8). To conduct a proper validation we calculated the average of the all available AERONET AOD retrievals for each station during the 24 h period that pertained to the daily AOD composite. In other words, we are comparing daily averaged AOD retrievals from AERONET to the daily AOD composite. Overall, our AOD composite compares closely to the AERONET AOD with a high correlation coefficient of 0.93. The outlier point where our AOD product is significantly higher than AERONET is likely caused by the fact that the pollution model was utilized instead of the desert dust model. The dust from the China deserts was able to propagate over this AERONET station in South Korea without significantly interacting with pollution.

6 Conclusions

The primary goal of this study was to generate a NRT daily AOD composite product that combines GEO and LEO satellite observations to assist with monitoring and tracking the trans-Pacific transport of aerosol plumes. In this paper, we present examples of the AOD composite product for a case study of trans-Pacific transport of Asian aerosols in mid-March 2014. Although the MODIS and VIIRS LEO satellites generally provide high-quality AOD retrievals (excluding the polar region), they have limited chances of observing pixels unaffected by clouds and sun glint where good retrievals can be made. Thus, we take advantage of the high temporal resolution of the GOES-15 and MTSAT-2 GEO satellites by developing AOD retrieval algorithms for each of them based on the continental and desert aerosol models in the 6SV1.1 RTM. We also develop a unique cloud/dust detection algorithm utilizing spectral, spatial, and

AMTD
8, 10319–10360, 2015

temporal techniques to disregard cloud contaminated pixels and locate dust pixels for the desert aerosol model. Overall, when combining GOES and MTSAT AOD retrievals with MODIS and VIIRS, we generated a daily AOD composite product that provided a more comprehensive understanding of the spatial distribution of aerosols across the Pacific Ocean. For the case study presented in this paper, we showed that the full extent of aerosol plumes propagating from Asia to the western Pacific were able to be recognized after incorporating the MTSAT AOD retrievals into the composite product. Additionally, the incorporation of the 6SV desert model into our AOD retrieval algorithms allowed for MTSAT to depict dust aerosol activity over the Gobi and Taklamakan deserts that was not shown by MODIS and VIIRS AOD. After crossing into the eastern Pacific, the extent of aerosol plumes are better represented by including GOES AOD retrievals into the new composite product.

Although the AOD composite product showed an overall good representation of the aerosol activity over our domain from Asia to North America, we noted several issues pertaining to the MTSAT and GOES AOD retrievals. We showed that high biases in AOD can appear in the tropical Pacific due to cloud artifacts impacting the GEO retrievals, which were more apparent over the tropical western Pacific than over the tropical eastern Pacific. However, we also found that biases in AOD can arise from the 28 day composite technique contained within the R_{sfc} retrieval procedure. The variation in solar geometry during the 28 day composite technique can lead to uncertainties in AOD of up to 34 % over areas of minimal R_{sfc} such as the tropical Pacific. Conversely, we found that MTSAT and GOES AOD retrievals are generally biased low across the northern Pacific from cloud artifacts impacting the R_{sfc} retrieval procedure. We did not discuss uncertainties in the GOES AOD retrieval algorithm over land as we are mostly concerned with tracking the aerosol plumes during their transport to the west coast of North America. Nevertheless, our assessment of the GOES AOD retrieval algorithm over land showed that it performs adequately over the west coast of the United States.

In this paper, we did not show examples of the 6 hourly AOD composite product, but it is important to note that the GEO AOD retrievals have a greater impact on this product,

AMTD
8, 10319–10360, 2015

since LEO satellites have limited coverage across our domain during the 6 h time window. The 6 hourly product can have important implications for aerosol forecasting as the shorter time window is more appropriate for the AOD assimilation process. Thus, the assimilation of both LEO and GEO satellite AOD retrievals can provide a more comprehensive coverage of AOD into chemistry models (e.g., Weather Research and Forecasting coupled with Chemistry (WRF-Chem)), which can help improve the representation of the simulated aerosol fields. This can ultimately improve air quality forecasts and the simulation of the aerosol-cloud-precipitation processes.

The future capability of GEO satellites for monitoring and tracking aerosol plumes will be greatly enhanced with the upcoming launch of the next-generation NOAA GOES-R and recently launched JMA Himawari satellites. These advanced GEO satellites carry instruments consisting of 16 spectral bands with 0.5 km spatial resolution at nadir for the 0.64 µm visible band while performing full disk scans every 5 min. Uncertainties associated with GEO AOD retrievals will be greatly reduced when using GOES-R and Himawari measurements. Also, the much improved spatial resolution of these satellites will help track aerosol plumes across the northern Pacific. This paper showed that GOES-15 and MTSAT-2 do not have adequate spatial resolution to track aerosol plumes in the northern parts of the Pacific. The very high temporal resolution of 5 min for the new generation satellites will also lead to a more complete understanding of the aerosol spatial distribution across the Pacific.

Acknowledgement. The MODIS Level 2 AOD products were downloaded from the Land, Atmosphere Near real-time Capability for EOS (LANCE) system operated by the NASA/GSFC/Earth Science Data and Information System (ESDIS) with funding provided by NASA/HQ. AOD from the VIIRS aerosol Environmental Data Record was downloaded using the NOAA Comprehensive Large Array-Data Stewardship System (CLASS) subscription service. The CALIPSO data was obtained from the NASA Langley Research Center Atmospheric Science Data Center.

AMTD
8, 10319–10360, 2015

References

Ackerman, S. A.: Remote sensing aerosols using satellite infrared observations, J. Geophys. Res., 102, 17069–17079, 1997.

Ackerman, S., Strabala, K., Menzel, P., Frey, R., Moeller, C., Gumley, L., Baum, B., Seemann, S. W., and Zhang, H.: Discriminating clear-sky from cloud with MODIS: algorithm theoretical basis document (MOD35), version 5.0, NASA Goddard Space Flight Cent., Greenbelt, MD, USA, 2006.

Ault, A. P., Williams, C. R., White, A. B., Neiman, P. J., Creamean, J. M., Gaston, C. J., Ralph, F. M., and Prather, K. A.: Detection of Asian dust in California orographic precipitation, J. Geophys. Res., 116, D16205, doi:10.1029/2010JD015351, 2011.

Diner, D. J., Beckert, J. C., Bothwell, G. W., and Rodrigues, J. I.: Performance of the MISR instrument during its first 20 months in Earth orbit, IEEE T. Geosci. Remote, 40, 1449–1466, 2002.

Dubovik, O., Smirnov, A., Holben, B. N., King, M. D., Kaufman, Y. J., Eck, T. F., and Slutsker, I.: Accuracy assessments of aerosol optical properties retrieved from Aerosol Robotic Network (AERONET) Sun and sky radiance measurements, J. Geophys. Res., 105, 9791–9806, 2000.

Gong, S. L., Zhang, X. Y., Zhao, T. L., Zhang, X. B., Barrie, L. A., McKendry, I. G., and Zhao, C. S.: A simulated climatology of Asian dust aerosol and its trans-Pacific transport. Part II: Interannual variability and climate connections, J. Climate, 19, 104–122, 2006.

Green, M., Kondragunta, S., Ciren, P., and Xu, C.: Comparison of GOES and MODIS aerosol optical depth (AOD) to aerosol robotic network (AERONET) AOD and IMPROVE $PM_{2.5}$ mass at Bondville, Illinois, J. Air Waste Manage., 59, 1082–1091, 2009.

Hillger, D., Kopp, T., Lee, T., Lindsey, D., Seaman, S., Miller, S., Solbrig, J., Kidder, S., Bachmeier, S., Jasmin, T., and Rink, T.: First-Light Imagery from Suomi NPP VIIRS, B. Am. Meteorol. Soc., 94, 1019–1029, 2013.

Holben, B. N., Eck, T. F., Slutsker, I., Tanŕe, D., Buis, J. P., Setzer, A., Vermote, E., Reagan, J. A., Kaufman, Y. J., Nakajima, T., Lavenu, F., Jankowiak, I., and Smirnov, A.: AERONET – A federated instrument network and data archive for aerosol characterization, Remote Sens. Environ., 66, 1–16, 1998.

AMTD
8, 10319–10360, 2015

Ignatov, A. and Stowe, L.: Aerosol retrievals from individual AVHRR channels. Part I: Retrieval algorithm and transition from Dave to 6S radiative transfer model, J. Atmos. Sci., 59, 313–334, 2002.

Jackson, J., Liu, H., Laszlo, I., Kondragunta, S., Remer, L. A., Huang, J., and Huang, H.-C.: Suomi-NPP VIIRS Aerosol Algorithms and Data Products, J. Geophys. Res., 118, 12673–12689, doi:10.1002/2013JD020449, 2013.

Jones, P. D., New, M., Parker, D. E., Martin, S., and Rigor, I. G.: Surface air temperature and its changes over the past 150 years, Rev. Geophys., 37, 173–199, 1999.

Kahn, R. A., Gaitley, B. J., Martonchik, J. V., Diner, D. J., Crean, K. A., and Holben, B.: Multiangle Imaging Spectroradiometer (MISR) global aerosol optical depth validation based on 2 years of coincident Aerosol Robotic Network (AERONET) observations, J. Geophys. Res., 110, D10S04, doi:10.1029/2004JD004706, 2005.

Khain, A., Rosenfeld, D., and Pokrovsky, A.: Aerosol impact on the dynamics and microphysics of deep convective clouds, Q. J. Roy. Meteor. Soc., 131, 2639–2663, 2005.

Knapp, K. R., Frouin, R., Kondragunta, S., and Prados, A. I.: Towards aerosol optical Depth retrievals over land from GOES visible radiances: determining surface reflectance, Int. J. Remote Sens., 26, 4097–4116, 2005.

Kotchenova, S. Y., Vermote, E. F., Matarrese, R., and Klemm Jr., F.: Validation of a vector version of the 6S radiative transfer code for atmospheric correction of satellite data. Part I: Path radiance, Appl. Optics, 45, 6762–6774, 2006.

Kotchenova, S. Y. and Vermote, E. F.: Validation of a vector version of the 6S radiative transfer code for atmospheric correction of satellite data. Part II: Homogeneous Lambertian and anisotropic surfaces, Appl. Optics, 46, 4455–4464, 2007.

Levy, R. C., Remer, L. A., Mattoo, S., Vermote, E. F., and Kaufman, Y. J.: Second-generation operational algorithm: retrieval of aerosol properties over land from inversion of Moderate Resolution Imaging Spectroradiometer spectral reflectance, J. Geophys. Res., 112, D13211, doi:10.1029/2006JD007811, 2007.

Levy, R. C., Remer, L. A., Kleidman, R. G., Mattoo, S., Ichoku, C., Kahn, R., and Eck, T. F.: Global evaluation of the Collection 5 MODIS dark-target aerosol products over land, Atmos. Chem. Phys., 10, 10399–10420, doi:10.5194/acp-10-10399-2010, 2010.

Liu, H., Remer, L. A., Huang, J., Huang, H.-C., Kondragunta, S., Laszlo, I., Oo, M., and Jackson, J. M.: Preliminary evaluation of S-NPP VIIRS aerosol optical thickness, J. Geophys. Res., 119, 3942–3962, 2014.

AMTD
8, 10319–10360, 2015

Mace, G. G., Zhang, Q., Vaughan, M., Marchand, R., Stephens, G., Trepte, C., and Winker, D.: A description of hydrometer layer occurrence statistics derived from the first year of merged Cloudsat and CALIPSO data, J. Geophys. Res., 114, D00A26, doi:10.1029/2007JD009755, 2009.

Mecikalski, J. R., MacKenzie Jr., W. M., König, M., and Muller, S.: Cloud-top properties of growing cumulus prior to convective initiation as measured by Meteosat second generation. Part II: Use of visible reflectance, J. Appl. Meteorol. Clim., 49, 2544–2558, 2010.

Naeger, A. R., Christopher, S. A., and Johnson, B. T.: Multiplatform analysis of the radiative effects and heating rates for an intense dust storm on 21 June 2007, J. Geophys. Res., 118, 9316–9329, 2013a.

Naeger, A. R., Christopher, S. A., Ferrare, R., and Liu, Z.: A new technique using infrared satellite measurements to improve the accuracy of the CALIPSO cloud-aerosol discrimination method, IEEE T. Geosci. Remote, 51, 642–653, 2013b.

Paciorek, C. J., Liu, Y., Macias, H. M., and Kondragunta, S.: Spatiotemporal associations between GOES aerosol optical depth retrievals and ground-level $PM_{2.5}$, Environ. Sci. Technol., 42, 5800–5806, 2008.

Pope, C. A., Burnett, R. T., Thun, M. J., Calle, E. E., Krewski, D., Ito, K., and Thurston, G. D.: Lung cancer, cardiopulmonary mortality, and long-term exposure to fine particulate air pollution, J. Amer. Med. Assoc., 287, 1132–1141, 2002.

Prados, A. I., Kondragunta, S., Ciren, P., and Knapp, K. R.: GOES Aerosol/Smoke Product (GASP) over North America: comparisons to AERONET and MODIS observations, J. Geophys. Res., 112, D15201, doi:10.1029/2006JD007968, 2007.

Remer, L. A., Kaufman, Y. J., Tanré, D., Mattoo, S., Chu, D. A., Martins, J. V., Li, R.-R., Ichoku, C., Levy, R. C., Kleidman, R. G., Eck, T. F., Vermote, E., and Holben, B. N.: The MODIS aerosol algorithm, products, and validation, J. Atmos. Sci., 62, 947–973, doi:10.1175/JAS3385.1, 2005.

Remer, L. A., Mattoo, S., Levy, R. C., and Munchak, L. A.: MODIS 3 km aerosol product: algorithm and global perspective, Atmos. Meas. Tech., 6, 1829–1844, doi:10.5194/amt-6-1829-2013, 2013.

Schmid, B., Michalsky, J., Halthore, R., Beauharnois, M., Harrison, L., Livingston, J., Russell, P., Holben, B., Eck, T., and Smirnov, A.: Comparison of aerosol optical depth from four solar radiometers during the fall 1997 ARM intensive observation period, Geophys. Res. Lett., 26, 2725–2728, 1999.

AMTD
8, 10319–10360, 2015

Shi, Y., Zhang, J., Reid, J. S., Liu, B., and Hyer, E. J.: Critical evaluation of cloud contamination in the MISR aerosol products using MODIS cloud mask products, Atmos. Meas. Tech., 7, 1791–1801, doi:10.5194/amt-7-1791-2014, 2014.

Sokolik, I. N.: The spectral radiative signature of wind-blown mineral dust: Implications for remote sensing in the thermal IR region, Geophys. Res. Lett., 29, 2154, doi:10.1029/2002GL015910, 2002.

Streets, D. G., Yarber, K. F., Woo, J.-H., and Carmichael, G. R.: Biomass burning in Asia: annual and seasonal estimates and atmospheric emissions, Global Biogeochem. Cy., 17, 1099, doi:10.1029/2003GB002040, 2003.

Talbot, R. W., Dibb, J. E., Lefer, B. L., Bradshaw, J. D., Sandholm, S. T., Blake, D. R., Blake, N. J., Sachse, G. W., Collins Jr., J. E., Heikes, B. G., Merrill, J. T., Gregory, G. L., Anderson, B. E., Singh, H. B., Thornton, D. C., Bandy, A. R., and Pueschel, R. F.: Chemical characteristics of continental outflow from Asia to the troposphere over the western Pacific Ocean during February–March 1994: Results from PEM-West B, J. Geophys. Res., 102, 28255–28274, doi:10.1029/96JD02340, 1997.

Toth, T. D., Zhang, J., Campbell, J. R., Reid, J. S., Shi, Y., Johnson, R. S., Smirnov, A., Vaughan, M. A., and Winker, D. M.: Investigating enhanced Aqua MODIS aerosol optical depth retrievals over the mid-to-high latitude Southern Oceans through intercomparison with co-located CALIOP, MAN, and AERONET data sets, J. Geophys. Res., 118, 4700–4714, 2013.

Vermote, E. F. and Kotchenova, S.: Atmospheric correction for the monitoring of land surfaces, J. Geophys. Res., 113, D23S90, doi:10.1029/2007JD009662, 2008.

Wilkening, K. E., Barrie, L. A., and Engle, M.: Transpacific air pollution, Science, 290, 65–67, 2000.

Winker, D. M., Pelon, J. R., and McCormick, M. P.: The CALIPSO mission: spaceborne lidar for observation of aerosols and clouds, Proc. SPIE, 4893, 1–11, 2003.

Winker, D. M., Pelon, J., Coakley Jr., J. A., Ackerman, S. A., Charlson, R. J., Colarco, P. R., Flamant, P., Fu, Q., Hoff, R. M., Kittaka, C., Kubar, T. L., Le Treut, H., McCormick, M. P., Mégie, G., Poole, L., Powell, K., Trepte, C., Vaughan, M. A., and Wielicki, B. A.: The CALIPSO Mission: a global 3D view of aerosols and clouds, B. Am. Meteorol. Soc., 91, 1211–1229, 2010.

AMTD
8, 10319–10360, 2015

Witek, M. L., Garay, M. J., Diner, D. J., and Smirnov, A.: Aerosol optical depths over oceans: a view from MISR retrievals and collocated MAN and AERONET in situ observations, J. Geophys. Res., 118, 12620–12633, 2013.

Yu, H., Remer, L. A., Chin, M., Bian, H., Tan, Q., Yuan, T., and Zhang, Y.: Aerosols from overseas rival domestic emissions over North America, Science, 337, 566–569, 2012.

Zhang, J., Reid, J. S., and Holben, B. N.: An analysis of potential cloud artifacts in MODIS over ocean aerosol optical thickness products, Geophys. Res. Lett., 32, L15803, doi:10.1029/2005GL023254, 2005.

Zhao, T. L., Gong, S. L., Zhang, X. Y., Blanchet, J. P., McKendry, I. G., and Zhou, Z. J.: A simulated climatology of Asian dust aerosol and its trans-Pacific transport. Part I: Mean climate and validation, J. Climate, 19, 88–103, 2006.

AMTD
8, 10319–10360, 2015

Table 1. Summary of satellites instruments used in producing the NRT AOD product.

Satellite Instrument	Latency (min)	Spectral Bands	Repeat Coverage	Swath width (km)	Local Equator Crossing Time	Spatial resolution (at nadir)	Visible bands for 550 nm AOD retrieval	AOD uncertainty
Aqua/Terra MODIS	90	36	1 to 2 days	2330	Aqua – 1030 Terra – 1330	$10 \times 10\,km^2$	Band 1: 620–670 nm Band 3: 459–479 nm	$\pm 0.03 \pm 0.05 \times$ AOD over ocean
S-NPP VIIRS	420	22	daily	3000	1330	$6 \times 6\,km^2$	Band M5: 662–682 nm Band M3: 478–488 nm	See MODIS
GOES-15 Imager	30	5	30 min	N/A	N/A	$4 \times 4\,km^2$	Band 1: 533–709 nm	18–34 %; lower uncertainty over water
MTSAT-2 Imager	30	5	30 min	N/A	N/A	$5 \times 5\,km^2$	Band 1: 540–816 nm	See GOES-15

AMTD
8, 10319–10360, 2015

Table 2. Average difference between observed ρ_{sat} and 6SV ρ_{toa} for the 24 cases along with RMS error for each aerosol model.

Aerosol Type	ρ_{sat} (%) – ρ_{toa} (%)	RMS error (%)
Desert	−3.45	3.84
Urban	4.86	5.79
Continental	−0.09	1.31
Maritime	−4.79	5.7
Biomass	−1.63	1.9
Pure Dust	4.19	5.84
Dust/Soot	10.2	11.17

AMTD
8, 10319–10360, 2015

Table 3. MTSAT cloud clearing algorithm with the various techniques and thresholds in the left column, center column shows the conditions when the techniques are used, and technique # relating to cloud/dust detection algorithm results in Fig. 2c are in the right column.

MTSAT cloud/dust detection algorithm		
Techniques	Condition	#
Spectral Techniques		
3.8–0.68 µm < −20 %	Land/Water	1
3.8–12.0 µm > 25 K	Land	2
3.8–12.0 µm > 12 K	Water	2
10.8–12.0 µm > 2.0 K and 3.8–10.8 µm > 2.0 K	Water	3
Spatial Techniques		
$3 \times 3\sigma$ 10.8 µm > 4.0 K or $3 \times 3\sigma$ 12.0 µm > 4.0 K	Land	4
$3 \times 3\sigma$ 10.8 µm > 1.0 K or $3 \times 3\sigma$ 12.0 µm > 1.0 K	Water	4
$3 \times 3\sigma$ 0.68 µm > 3.0 % or $5 \times 5\sigma$ 0.68 µm > 3.0 %	Land	5
$3 \times 3\sigma$ 0.68 µm > 1.5 % or $5 \times 5\sigma$ 0.68 µm > 1.5 %	Water	5
Temporal Techniques		
10.8 μm_{time} > 3.0 K or 12.0 μm_{time} > 3.0 K	Water	6
10.8 μm_{time} > 10.0 K and 12.0 μm_{time}/10.8 μm_{time} > 1.0 K	Land	6
Dust Techniques		
10.8–12.0 µm < −1.0 K	Cloud	7
$3 \times 3\sigma$ 0.68 µm < 4.0 % and $5 \times 5\sigma$ 0.68 µm < 4.0 %	Cloud	7
3.8–10.8 µm > 4.0 K	Cloud	7
12.0 µm > 258 K	Cloud	7
10.8–12.0 µm <= −0.5 K or R_{sfc} > 20 %	Cloud-free	8

AMTD
8, 10319–10360, 2015

Table 4. The coverage for the daily AOD composite maps when only LEO (MODIS/VIIRS) and GEO (MTSAT/GOES) sensors are considered compared to when both LEO and GEO sensors are considered (COMP) in our final product. We present the coverage statistics for six days including the 18 and 23 March case studies analyzed in this paper. The number of valid AOD retrievals across our AOD composite domain along with the percent coverage based on the total number of available grid boxes are shown.

Case	LEO coverage (# pixels/%)	GEO coverage (# pixels/%)	COMP coverage (# pixels/%)
18 Mar	48 368/69	43 906/62	58 564/83
19 Mar	49 980/71	45 023/64	60 050/85
20 Mar	46 543/66	41 348/59	55 792/79
21 Mar	50 071/71	44 998/64	61 755/88
22 Mar	43 851/62	39 004/55	52 095/74
23 Mar	44 960/64	40 540/58	53 580/76
Average	47 296/67	42 470/60	56 973/81

AMTD
8, 10319–10360, 2015

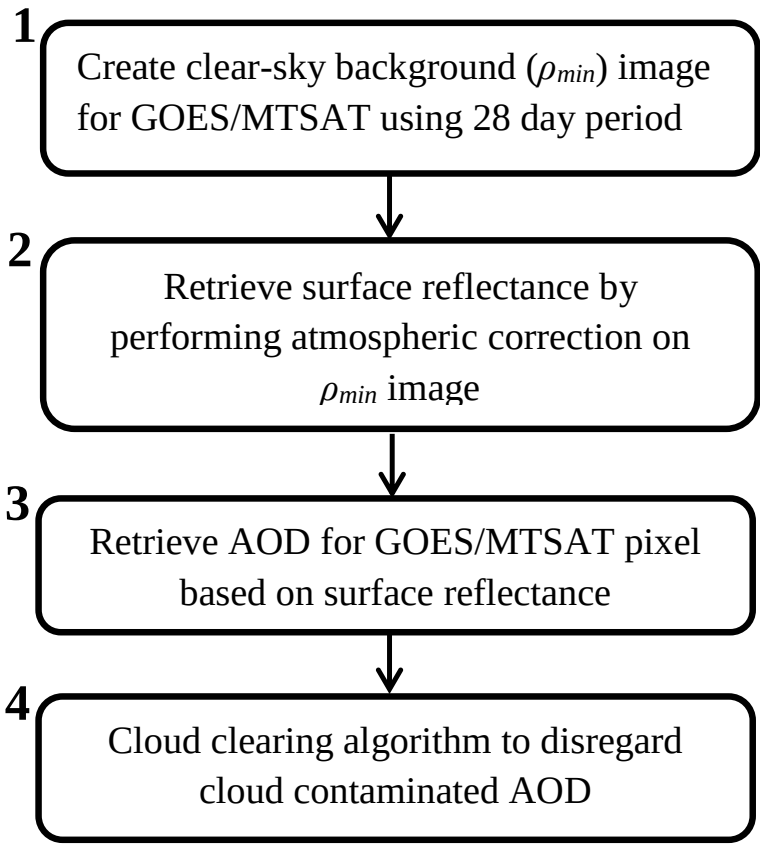

Figure 1. Four major steps involved in our GOES and MTSAT AOD retrieval algorithms.

AMTD
8, 10319–10360, 2015

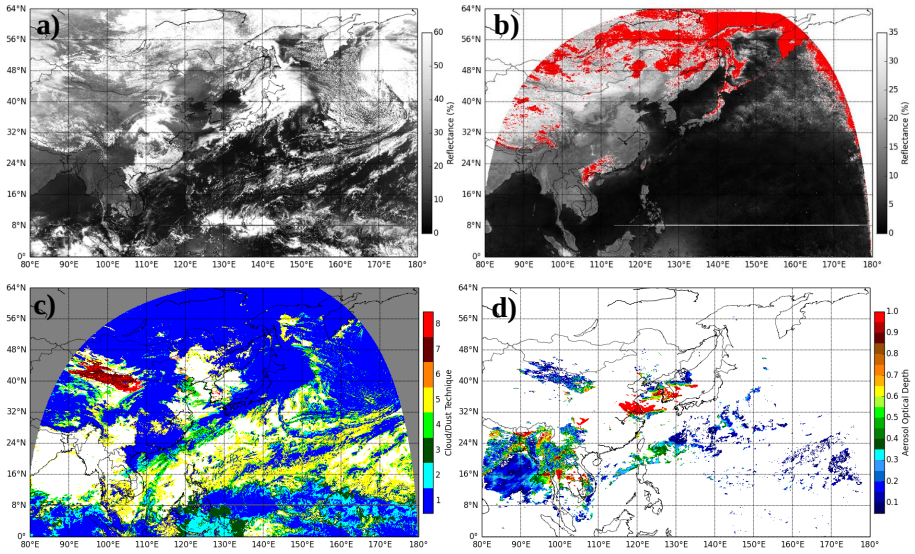

Figure 2. All panels pertain to 18 March 2014 at 05:01 UTC. **(a)** MTSAT-2 0.68μm reflectance image. **(b)** R_{sfc} retrievals for each valid pixel in MTSAT-2 scan where pixels having $R_{sfc} > 35\,\%$ are denoted in red. **(c)** Cloud/dust detection results where the colorbar labels relate to technique # in Table 3. **(d)** MTSAT AOD retrievals.

AMTD
8, 10319–10360, 2015

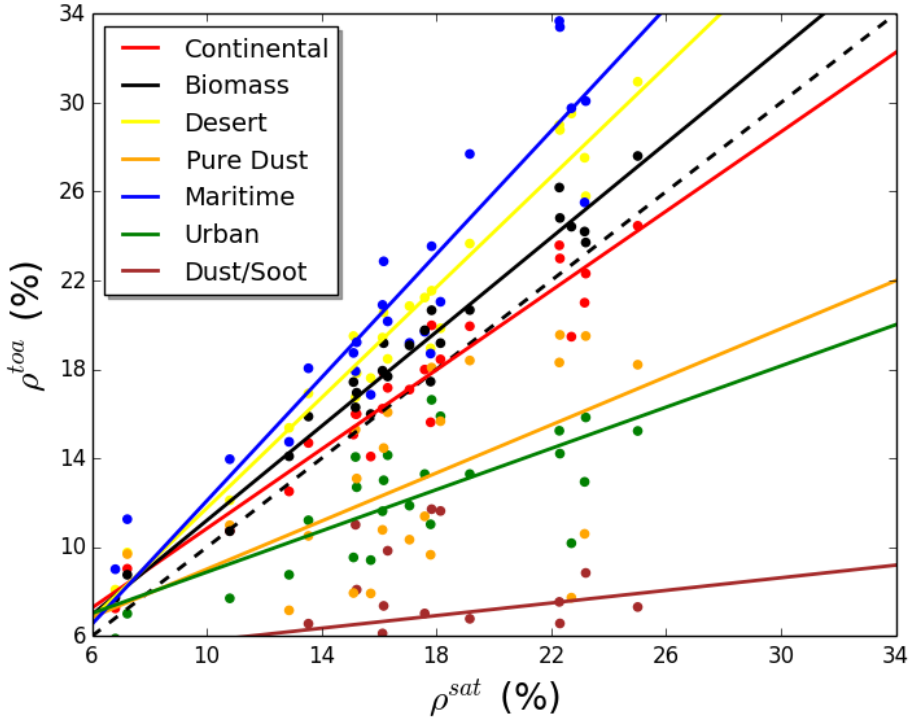

Figure 3. Observed ρ_{sat} vs. 6SV ρ_{toa} results for 24 unique non-desert cases over eastern Asia during March and April 2014 where seven different aerosol models were tested for each case. Dust and pollution were the primary aerosol constituents during this period.

AMTD
8, 10319–10360, 2015

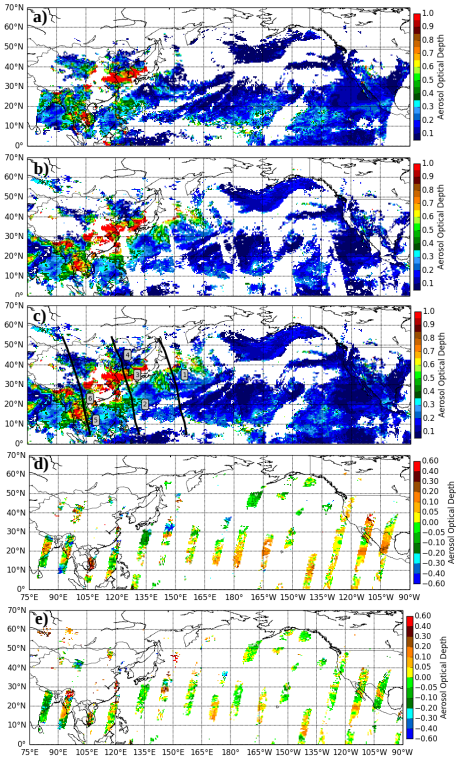

Figure 4. The top three panels display the daily AOD composites valid at 00:00 UTC on 18 March 2014. **(a)** Example of the daily AOD composite when only MTSAT/GOES retrievals are utilized, **(b)** example of when only MODIS/VIIRS retrievals are utilized, **(c)** final version of our daily AOD composite product that combines all satellite retrievals onto the same map. **(d)** Difference plot between the MTSAT/GOES AOD composite product and available MISR AOD retrievals during the 24 h period. **(e)** Difference plot between MODIS/VIIRS AOD composite product and MISR AOD.

AMTD
8, 10319–10360, 2015

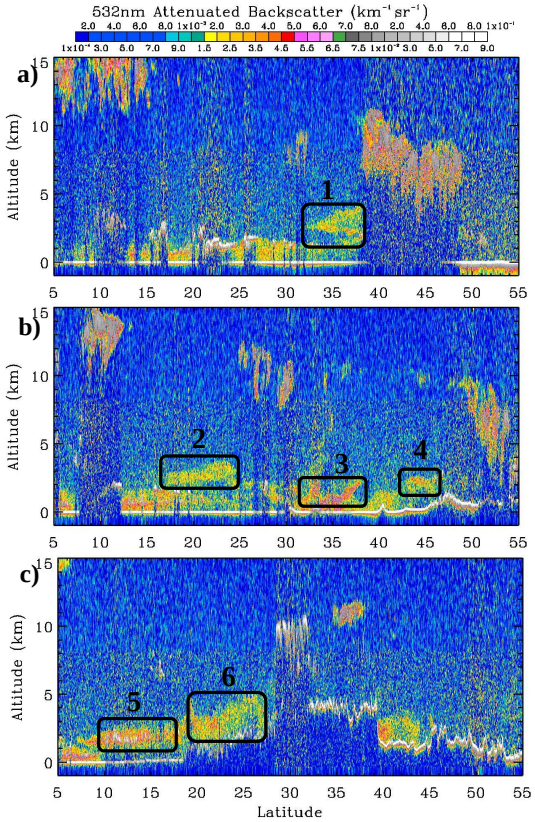

Figure 5. All panels show CALIPSO 532 nm attenuated backscatter profiles on 18 March 2014. CALIPSO transects are indicated in Fig. 4c (black lines), which are increasing in time from east to west with **(a)** at about 03:20 UTC, **(b)** at about 05:00 UTC, and **(c)** at about 06:40 UTC. Boxes highlight regions of interest. The location of these boxes along the CALIPSO transects are also indicated in Fig. 4c.

AMTD
8, 10319–10360, 2015

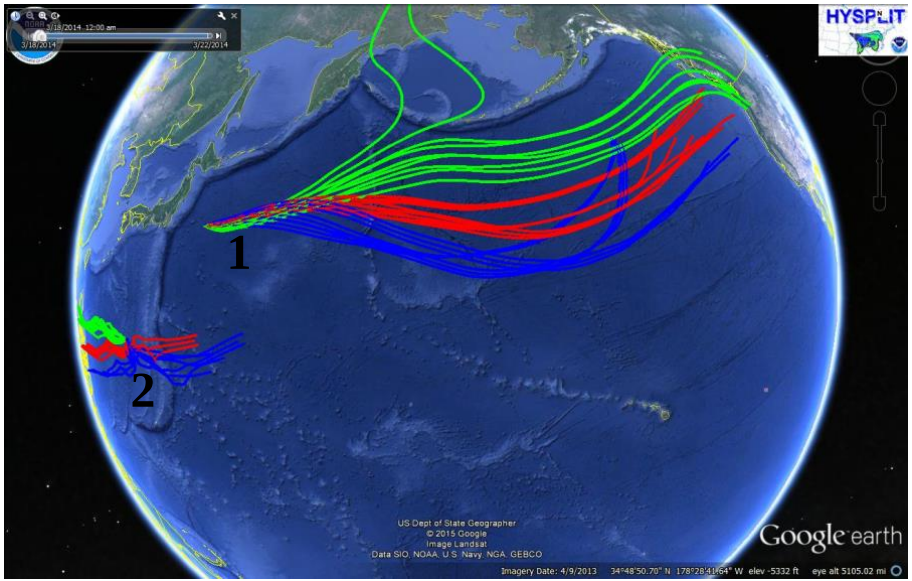

Figure 6. NOAA HYSPLIT model forward trajectory results for 4 day time period beginning 18 March 2014 at 05:00 UTC. We initialize the model from locations 1, 2, and 5 along the the CALIPSO transects in Fig. 5. CALIPSO aerosol height information at these locations are also used to initialize the model. Location 5 was initialized over Southeast Asia and all the forward trajectories took the aerosol plume south and west, thus, the trajectories never entered the Google Earth display region shown here.

AMTD
8, 10319–10360, 2015

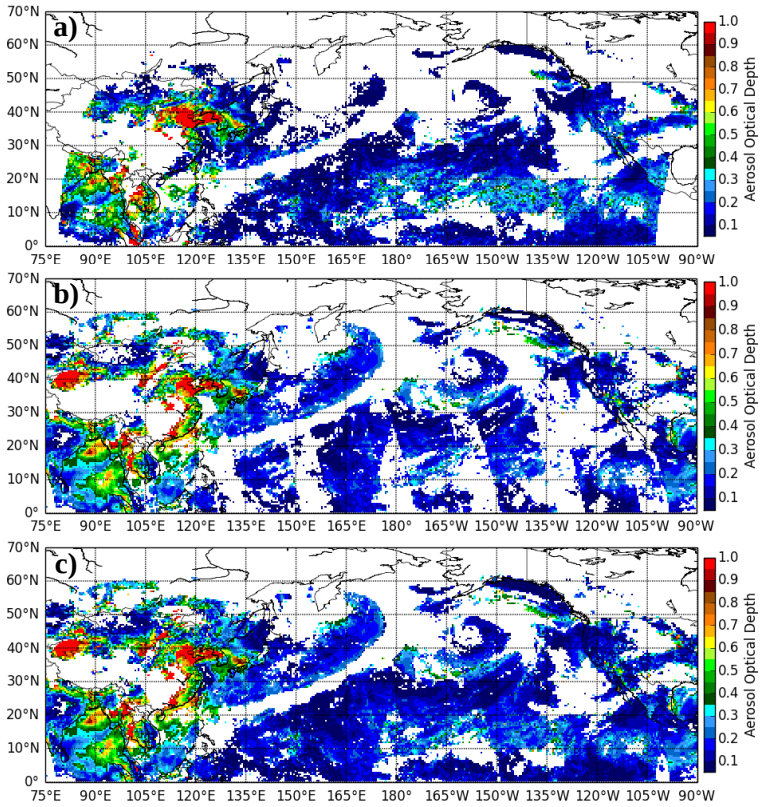

Figure 7. Panels show the daily AOD composites valid at 00:00 UTC on 23 March 2014. **(a)** Example of the daily AOD composite when only MTSAT/GOES retrievals are utilized, **(b)** example of when only MODIS/VIIRS retrievals are utilized, **(c)** final version of our daily AOD composite product.

AMTD
8, 10319–10360, 2015

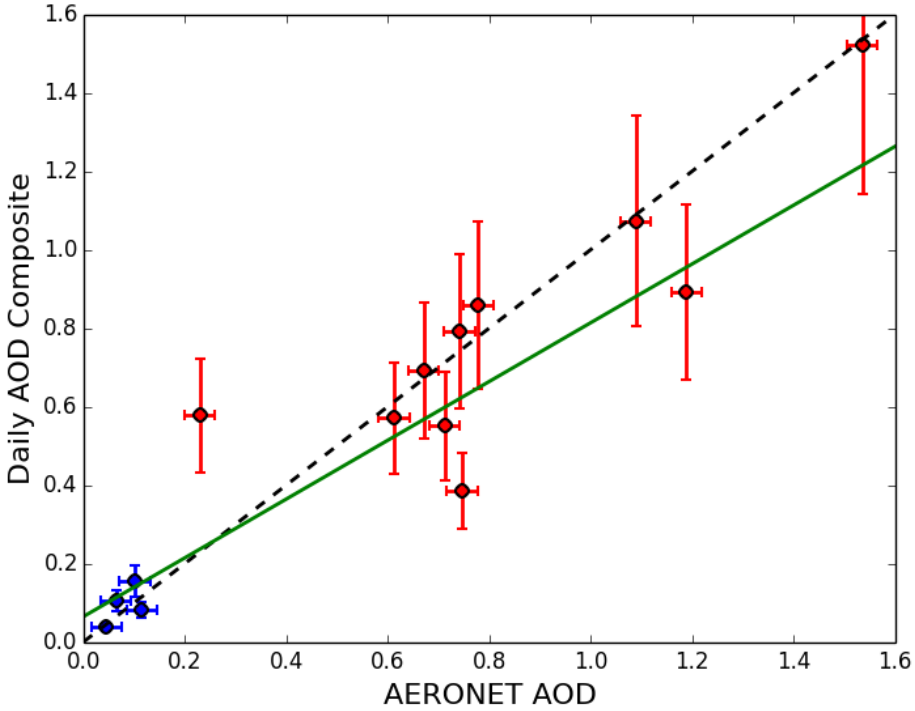

Figure 8. Average of level 1.5 AERONET AOD retrievals from 17 March at 12:00 UTC to 18 March at 12:00 UTC vs. our daily AOD composite product valid on 18 March 2014 at 00:00 UTC. AERONET AOD from 10 stations in East Asia (red) and 4 stations along the west coast of the United States (blue) were used to validate the daily AOD product. Error bars are based on ±0.015 uncertainty for AERONET AOD retrievals and 25 % uncertainty for the daily AOD composite. The 25 % uncertainty is simply the average of the GEO uncertainty range (18–34 %).

AMTD
8, 10319–10360, 2015